Adipocyte-derived endotrophin promotes malignant tumor progression

Jiyoung Park[1] and Philipp E. Scherer[1,2,3]

[1]Touchstone Diabetes Center, Department of Internal Medicine, [2]Department of Cell Biology, and [3]Simmons Cancer Center, University of Texas Southwestern Medical Center, Dallas, Texas, USA.

Adipocytes represent a major cell type in the mammary tumor microenvironment and are important for tumor growth. Collagen VI (COL6) is highly expressed in adipose tissue, upregulated in the obese state, and enriched in breast cancer lesions and is a stimulator of mammary tumor growth. Here, we have described a cleavage product of the COL6α3 chain, endotrophin (ETP), which serves as the major mediator of the COL6-mediated tumor effects. ETP augmented fibrosis, angiogenesis, and inflammation through recruitment of macrophages and endothelial cells. Moreover, ETP expression was associated with aggressive mammary tumor growth and high metastatic growth. These effects were partially mediated through enhanced TGF-β signaling, which contributes to tissue fibrosis and epithelial-mesenchymal transition (EMT) of tumor cells. Our results highlight the crucial role of ETP as an obesity-associated factor that promotes tumor growth in the context of adipocyte interactions with tumor and stromal cells.

Introduction

Breast cancer is the most common malignancy found in women. Among a number of risk factors, obesity ranks high and contributes significantly to postmenopausal breast cancer risk (1). Epidemiological evidence supports a tight association among obesity, cancer incidence, and mortality (2). Hence, the adipocyte, as a major constituent of the mammary tumor stroma (3), is a likely contributor to tumor growth. The interactions between malignant epithelial cancer cells and the surrounding stromal cells have a profound impact on tumor physiology, including cell growth, survival, metastasis, and recurrence (4). Numerous studies have documented contributions of stromal cells to tumor growth, through factors released from tumor-associated macrophages, fibroblasts, and endothelial cells (5–7). However, less is known about adipocyte factors that dominate the tumor microenvironment; such factors are either permissive or, in some cases, actively contributing to tumor cell growth (8).

The adipocyte is an established endocrine organ, secreting various signaling molecules — such as adipokines, chemokines, and extracellular matrix (ECM) constituents — in response to nutritional or hormonal stimuli (9). Adipocyte-derived factors involved in tumor progression include proteins such as adiponectin, leptin, TNF-α, monocyte chemotactic protein–1 (MCP-1), IL-6, and ECM components that control tumor cell behavior within the tumor microenvironment. Key signaling networks associated with cell proliferation, angiogenesis, inflammation, and apoptosis are activated by adipokines; these include PI3K, ERK1/2, STAT3, and NF-κB (10). Such pathways are frequently activated in tumor tissues (11).

Collagen type VI (COL6; encoded by *Col6a1*, *Col6a2*, and *Col6a3*) is ubiquitously expressed throughout connective tissues, such as blood vessels, muscle, lung, and skin. However, adipose tissue (AT) is the most abundant source of COL6 (12). COL6 is a large collagenous glycoprotein composed of 3 chains, α1, α2, and α3, that are intracellularly assembled from heterotrimeric monomers to tetramers (13). Once secreted into the extracellular space, COL6 tetramers associate into microfibrils. Subsequently, the carboxy-terminal C5 domain of the α3 chain is proteolytically cleaved off from the COL6 microfibrils (14). However, the details of this cleavage event and the functional role of the cleavage product, the C5 domain, remain unknown, with the exception that the C5 domain plays an important structural role for COL6 microfibril formation (15). Our previous studies have shown that adipocyte-derived COL6 is a tumor-promoting factor (16) and that COL6-knockout (*Col6a1*$^{-/-}$) mice — in the background of the mammary tumor virus–polyoma middle T antigen (MMTV-PyMT) mammary tumor mouse model (referred to herein as PyMT mice; ref. 17) — exhibit attenuated formation of early hyperplasia and primary tumor growth (18). Notably, the carboxyterminal domain of the COL6α3 chain is stable and highly enriched in human breast cancer specimens compared with full-length COL6α3 (18). However, it remains unknown whether the cleaved C5 fragment of the COL6α3 chain, referred to herein as endotrophin (ETP), participates in mammary tumor progression.

Our studies explored whether ETP regulates tumor cell growth and metastasis on its own, independent of other COL6 subunits, or the remainder of the COL6α3 chain. It is widely appreciated that the ECM provides mechanical and structural support within the microenvironment. In addition, ECM-derived proteolytic fragments can directly activate various signaling pathways, influencing events in neighboring cells that express ECM receptors, such as integrins (19). To better define the role of ETP in tumor progression within the local tumor microenvironment, independent of the rest of the COL6 complex, we generated transgenic mice that harbor ETP with a signal sequence under the control of the mammary epithelial specific MMTV promoter. MMTV-ETP transgenic mice were characterized either independently (referred to herein as ETP mice), in the background of PyMT mice (PyMT/ETP mice), or with tumor implantations into isogenic mice. We used these mouse models in combination with specific ETP neutralizing antibodies to evaluate their therapeutic potential. The aim of our studies was to identify and define mechanisms responsible for the effects of COL6 on tumor growth and metastasis and further establish which signaling pathways play critical roles mediating the potent ETP effects.

Conflict of interest: The authors have declared that no conflict of interest exists.
Citation for this article: *J Clin Invest.* 2012;122(11):4243–4256. doi:10.1172/JCI63930.

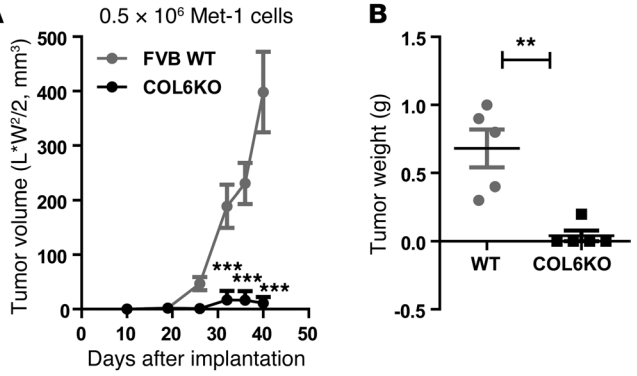

Figure 1
Regression of tumor growth in *Col6a1*$^{-/-}$ mice. Met-1 cells (0.5 × 10^6 cells/mouse) were implanted into either FVB WT or *Col6a1*$^{-/-}$ (COL6KO) mice (mean ± SEM; $n = 5$ per group). (**A**) Tumor volume, determined by caliper measurements. ***$P < 0.001$ vs. WT, 2-way ANOVA. (**B**) Tumor weight. **$P = 0.0022$ vs. WT, unpaired t test.

Results

Host-derived COL6 is required to support mammary epithelial cancer cell growth. In order to assess the effects of COL6 on mammary tumor progression, we determined mammary epithelial cancer cell growth in the *Col6a1*$^{-/-}$ mouse, which lacks a functional COL6A1 chain. This leads to the functional deficiency of the holo-COL6 heterotrimeric complex (20). The growth of the mouse mammary cancer cell line Met-1, originating from a PyMT mouse, was significantly attenuated in *Col6a1*$^{-/-}$ versus WT mice (Figure 1, A and B). Thus, the lack of functional COL6 in the tumor microenvironment led to a substantial reduction in mammary epithelial cancer cell growth.

ETP is abundant in tumor tissues. To further investigate a role of COL6 in tumor progression, particularly in the context of ETP, we generated polyclonal antibodies specific for either mouse or human ETP domains (Supplemental Figure 1, A and B); a substantial degree of conservation was preserved between the species (Figure 2A). Similar to holo-COL6 levels, secreted ETP was readily identified in conditioned media of 3T3-L1 adipocytes, but not 3T3-L1 fibroblasts (Figure 2B). Consistent with this observation, we observed high ETP levels in the AT of obese animals, such as *ob/ob* and *db/db* mice, compared with lean controls (Figure 2C). Interestingly, ETP prominently accumulated in obesity-associated crown-like structures of AT (Figure 2C, arrows), prominent structures in dysfunctional adipocytes in which infiltrating macrophages mediate chronic inflammatory responses (21). In contrast, a holo-COL6–specific antibody primarily highlighted a signal at the periphery of adipocytes (Supplemental Figure 2C). Immunostaining of tumor tissues from PyMT mice with anti–holo-COL6 showed that entire tumor lesions were surrounded by COL6 fibrils, with weaker staining observed in AT (Figure 2, D and G). Interestingly, cleaved soluble ETP freely diffused in the microenvironment and accumulated on primary tumor lesions of PyMT mice in a paracrine manner (Figure 2, E and G). Of note, ETP was less prominent on metastasized tumors in the lung (Figure 2F), which suggests that ETP levels on tumor cells may critically depend on the presence of local adipocytes to supply ETP. Histological analysis of human breast tumor tissues indicated that ETP was highly abundant on both epithelial cancer cells and various stromal cells within the tumor microenvironment, with a much lower signal seen in benign tissues (Figure 3A and Supplemental Figure 2A). In the mouse, ETP was highly expressed in the mammary epithelial cancer cell Met-1, relative to other cell types, such as the endothelial cell line MS-1 or primary macrophages (Supplemental Figure 2D). This suggests that cancer cells can express ETP, even though AT was the major source for COL6 among various WT tissues and PyMT tumor tissue (Supplemental Figure 2, E and F). ETP overexpression was not restricted to mammary cancer cells. We observed similar increases in ETP in other tumor sections, such as in human colon cancers, which showed significantly higher ETP levels than those in benign tissues (Figure 3B and Supplemental Figure 2B). ETP may therefore be a relevant player in several other tumor settings and may play a crucial role in cancer cell behavior through both paracrine and autocrine signaling.

To identify the tissues that are critical targets for ETP in circulation, we injected infrared fluorescent dye–labeled (IRD-800) recombinant ETP protein into PyMT mice through tail vein injection. The signal distribution in these tumor-bearing mice was compared with that of WT mice. The in vivo fate of the labeled ETP was monitored by fluorescence scanning. A high fluorescence signal was observed in liver and bladder of all mice due to clearance. However, ETP was predominantly observed in tumor lesions compared with control-labeled IgGs (Figure 3C). As determined by quantification, ETP was highly enriched in mammary tumor tissues relative to mammary glands of WT mice (Figure 3D).

Elevated local ETP levels convey higher antiapoptotic and promitotic indices in normal mammary epithelial cells. To directly explore the role of ETP in mammary tumor growth, we used a gain-of-function approach with a transgenic mouse model expressing ETP under the control of MMTV promoter to elevate local ETP levels within the mammary gland. To achieve efficient ETP secretion, a prolactin signal sequence was inserted in-frame 5′ to the region encoding the mouse ETP sequence (Supplemental Figure 3A). ETP transgene levels were highly upregulated in a high-expressing line compared with the more modest overproduction of other low-expressing lines (Supplemental Figure 3B). Immunostaining with antibodies against ETP indicated that ETP was enriched in mammary ductal epithelium in both transgenic mouse lines relative to WT, whereas no ETP signal was detected in *Col6a1*$^{-/-}$ mice (Figure 4A).

Assessment of mammary gland development in ETP mice is critical to evaluate the roles of ETP in mammary tumor progression, as most primary mammary tumors originate from mammary ductal or intraductal epithelial cells. Histological analysis — including whole-mount, H&E, and Masson's Trichrome C staining — of mammary glands showed that ductal epithelial growth and the degree of fibrosis in both ETP transgenic lines was comparable to those in WT mice (Supplemental Figure 3, C–E). The final stages of mammary gland development are completed upon pregnancy, lactation, and involution (22). The high-expressing ETP line displayed a deficiency in fertility (Supplemental Figure 3F) and reduced locomotion (data not shown); these secondary effects of elevated ETP levels may make the interpretation of local findings within the mammary gland more challenging. We therefore focused on the low-expressing line and examined the process of involution. In this process, the secretory epithelial cells undergo apoptosis with concomitant redifferentiation of adipocytes, thereby reconstituting prepregnancy status after weaning. Involution was delayed at an early stage of the process in ETP mice (Supplemental Figure 3G), along with a reduction in apoptosis in secretory epithelial cells (Figure 4, B and C). This suggests that ETP

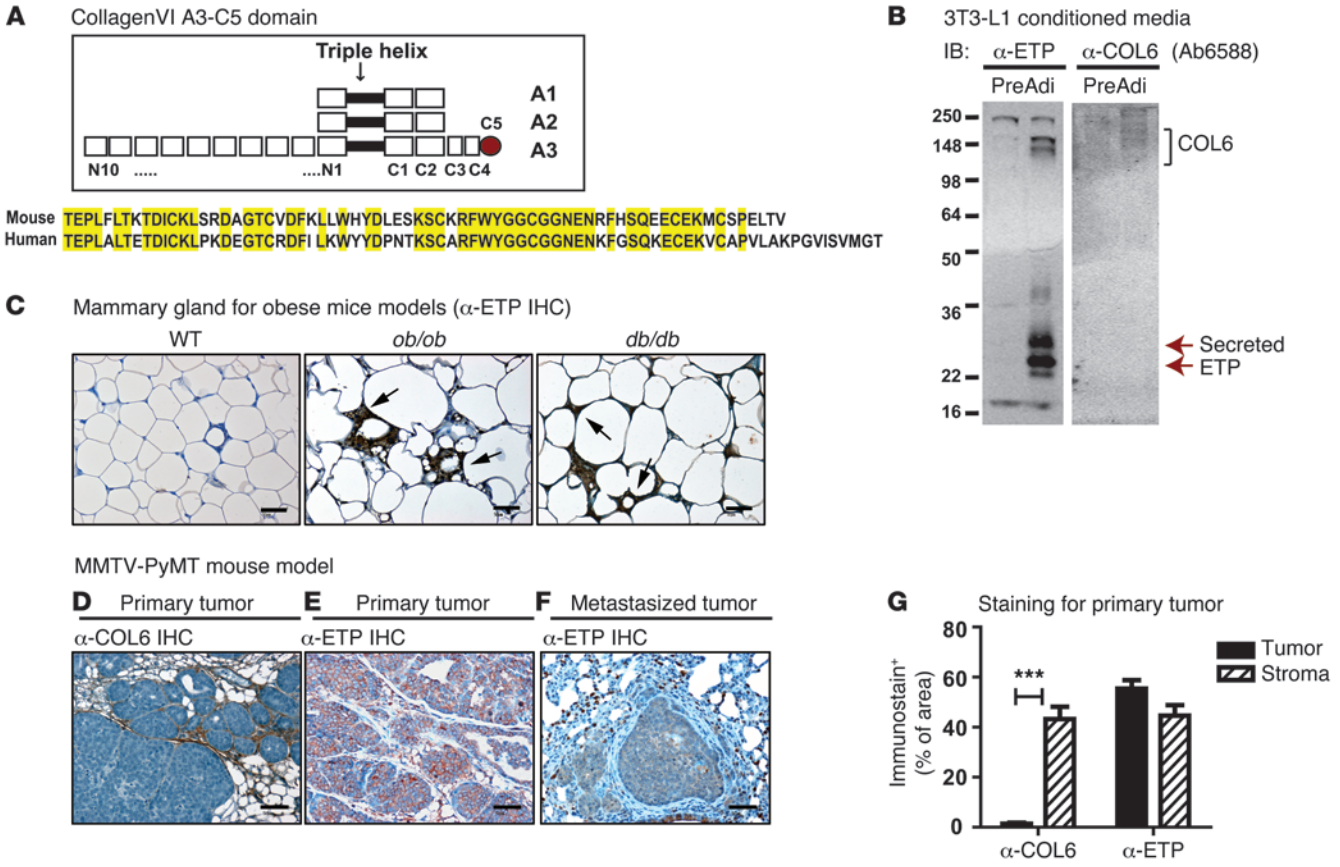

Figure 2

Expression profiles of ETP. (**A**) COL6 is composed of COL6α1, -α2, and -α3 chains. The C5 domain of the α3 chain, cleaved off the COL6 microfilament, is highlighted in red. Shown are amino acid sequences compared between the human and mouse COL6α3-C5 domain. Conserved sequences are highlighted in yellow. (**B**) Western blots showing abundant secretion of ETP from adipocytes. Conditioned media from 3T3-L1 preadipocytes and fully differentiated adipocytes were subjected to Western blotting using α-mETP and α-COL6. Arrows indicate the secreted form of ETP. (**C**) ETP immunostaining of mammary gland tissues from obese animals, *ob/ob* and *db/db* mice, compared with lean controls (n = 5 per group). Arrows indicate crown structure. Scale bars: 50 μm. (**D** and **E**) holo-COL6 and ETP immunostaining of tumor tissues from 9-week-old PyMT mice with α-COL6 (**D**) and α-mETP antibody (**E**), respectively. Lung tissues from 13-week-old PyMT mice were used for metastasized tumor lesions (**F**). Scale bars: 50 μm. (**G**) α-COL6– and α-ETP–positive staining area in tumor or stroma for the primary tumors. Data are mean ± SEM of multiple fields in n = 5 per group. ***P < 0.001 vs. tumor, unpaired t test.

acts as a potent antiapoptotic factor in this setting. Delays in the process of involution frequently resemble the prolonged survival of epithelial cells in a cancer setting. As a comparison, we observed an enhanced rate of involution in *Col6a1*$^{-/-}$ mice (Supplemental Figure 3G); concomitantly, apoptosis was increased approximately 2-fold in *Col6a1*$^{-/-}$ mice (Figure 4, B and C). Nevertheless, ETP mice did eventually revert back to prepregnancy status, albeit with delayed kinetics (Supplemental Figure 3G).

Abnormal developmental cues can induce and promote a cancerous transformation of mammary epithelial cells. Indeed, several mice with high ETP expression spontaneously developed tumors (Figure 4D). We did not observe spontaneous tumor formation in low ETP expressers or WT mice up to 18 months of age (data not shown). Immunostaining with Ki67 showed that cell proliferation was increased in hyperplastic lesions of mammary tissue in the high-expressing mice (Figure 4E), which suggests that high levels of ETP alone are sufficient to augment promitogenic activity. No lesions were observed in WT mice, and hence no detectable mitogenic activity or Ki67 signal was evident (Figure 4E). We therefore directed further efforts toward the physiologically more relevant lower-expressing ETP line, since these mice develop the mammary ductal epithelium completely normally and overexpress ETP only locally.

ETP augments tumor growth and metastasis in PyMT mice. To assess ETP function, we aimed to expose ETP mice to an additional tumorigenic trigger. For this purpose, we used the PyMT mouse, an aggressive mammary adenocarcinoma model that develops late-stage carcinoma and pulmonary metastasis within 15 weeks (23). Accumulated ETP levels in tumor tissues of PyMT/ETP mice were about 1.5-fold those of endogenous ETP in PyMT mice (Figure 5A), and the rate of early tumor growth was augmented in PyMT/ETP versus PyMT mice (Figure 5B). In light of high endogenous ETP levels accumulating locally as well, differences in late-stage tumors were not significant between the 2 groups when assayed by caliper measurements (Figure 5C). More striking differences were obtained at the level of metastasis (Figure 5, D and E). To more sensitively assess tumor growth, we generated a mouse model harboring the

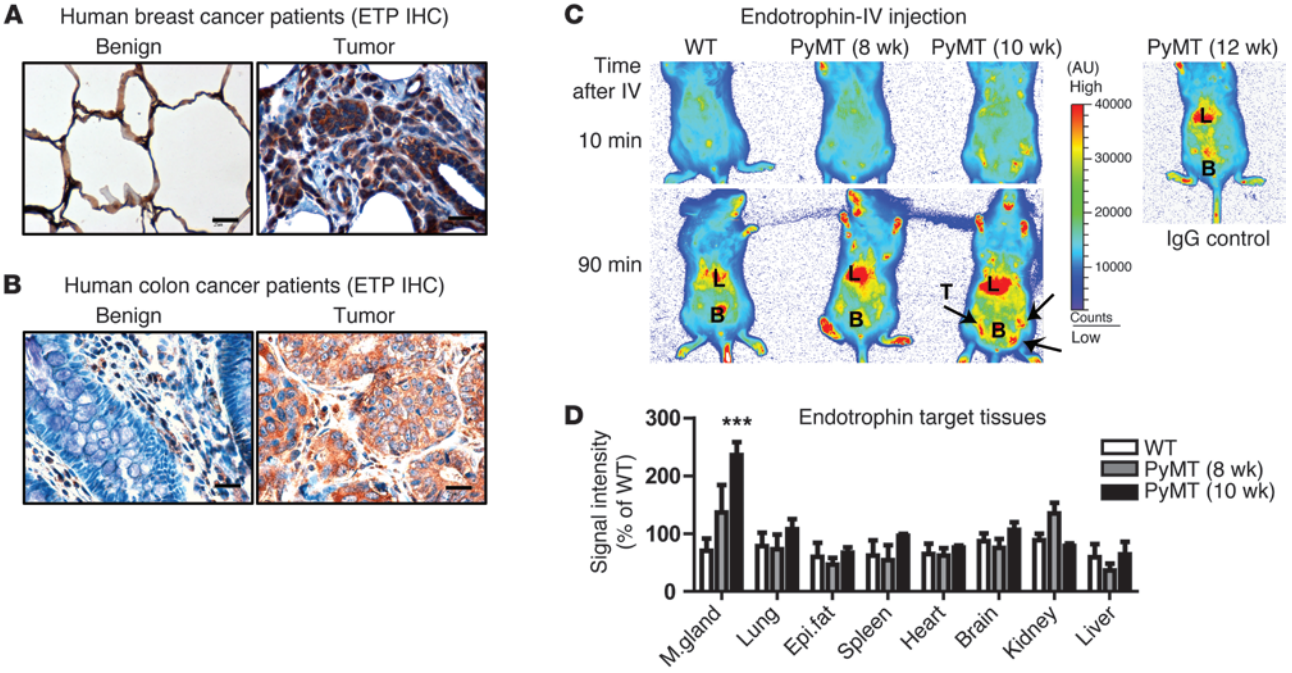

Figure 3

ETP levels in human cancer specimens and its target tissues. (**A** and **B**) Human cancer tissues compared with those of benign tissues were immunostained with human ETP–specific polyclonal antibody. Human samples for breast cancer (**A**) and colon cancer (**B**) were analyzed. Scale bars: 25 μm. (**C** and **D**) Whole body in vivo imaging of injected ETP. IRD-800 fluorescence–labeled ETP protein (10 μg) was intravenously injected into WT, 8-week-old PyMT, and 10-week-old PyMT mice by tail vein. (**C**) ETP levels were visualized by the Licor Infrared Scanner 10–90 minutes after injection. Arrows indicate mammary tumors. L, liver; B, bladder; T, tumor. IgG was used as a negative control. (**D**) Tissues were excised 2 hours after injection, and ETP-positive fluorescence signals were determined with a Licor Infrared Scanner. Quantified values were normalized to total area and represented as percentage of WT. ***$P < 0.001$.

infrared fluorescence transgene FP635 under the control of the MMTV promoter, which allowed us to monitor tumor growth longitudinally through in vivo imaging (Supplemental Figure 4A). Breeding this transgene into PyMT animals (referred to herein as FP635/PyMT mice) allowed us to readily assess tumor growth by whole-body fluorescence signal intensity, given that the infrared range allows deeper tissue penetration with reduced autofluorescence from surrounding AT (Supplemental Figure 4B). By assessing in vivo images, the differences of tumor burden between the FP635/PyMT/ETP and FP635/PyMT groups became apparent and significant (Figure 5F), which indicates that ETP not only promotes pulmonary metastasis, but also further enhances primary tumor growth. Ki67 staining at late stages did not show an increased frequency of proliferating cells in tumor tissues in PyMT/ETP versus PyMT animals (Figure 6A). Nevertheless, tumor tissue fibrosis at that age was doubled in PyMT/ETP versus PyMT mice (Figure 6B). Indeed, a subset of genes associated with tissue fibrosis, including several types of collagens, lysyl oxidase (*Lox*), and *TGF*β, as well as genes for epithelial-mesenchymal transition (EMT), such as fibroblast stimulating protein (*FSP1*) and vimentin, showed trends toward an increase in tumor tissues (Figure 6, E and F). More dramatic alterations were obtained in the area of tumor angiogenesis: ETP tumor tissues harbored a 3-fold increase in functional blood vessel area compared with controls (Figure 6C), with a concomitant reduction in hypoxia (Figure 6D). Markers for angiogenesis, such as *CD31*, *VEGFR2*, and *HIF1*α, were significantly upregulated in tumor tissues from PyMT/ETP mice. Moderate increases were observed in lymphangiogenesis markers, such as *VEGFc*, podoplanin (*Pdpn*), and the lymphatic vessel endothelial hyaluronan receptor (*LYVE-1*) (Figure 6G). These gene expression changes were consistent with the immunostains of tumor tissues for lymphangiogenesis, such as podoplanin (Figure 6C). Levels of inflammatory cytokines, such as *IL6* and *TNF*α, were moderately increased (Figure 6H). Taken together, these findings indicate that ETP enhances fibrosis, angiogenesis, and inflammation, all of which are known to promote primary tumor growth and metastasis (24).

ETP enhances the EMT process. To investigate gene expression alterations induced by ETP, we compared cDNA microarrays from size-adjusted tumor tissues from PyMT/ETP and PyMT mice. ETP-modulated genes fell primarily into categories of targets involved in key phosphorylation events, such as phosphatases, kinases, and other phosphoproteins (Supplemental Figure 5A). Furthermore, the most significantly altered canonical pathways modulated by ETP were associated with immune responses, cell cycle regulation, and stem cell pluripotency (Supplemental Figure 5B). Notably, stem cell–like pluripotency is a hallmark of cancer cells for survival and invasion, which is tightly linked to the process of EMT (24). Levels of the epithelial cell marker E-cadherin — the loss of which is a characteristic feature of EMT (25) — were significantly decreased in tumor tissues from PyMT/ETP relative to PyMT mice (Figure 7A), which suggests that ETP induces EMT. This enhanced EMT was consistent with the in vivo phenotype: the metastatic burden was prominently increased in PyMT/ETP versus PyMT mice (Figure 5, D–F).

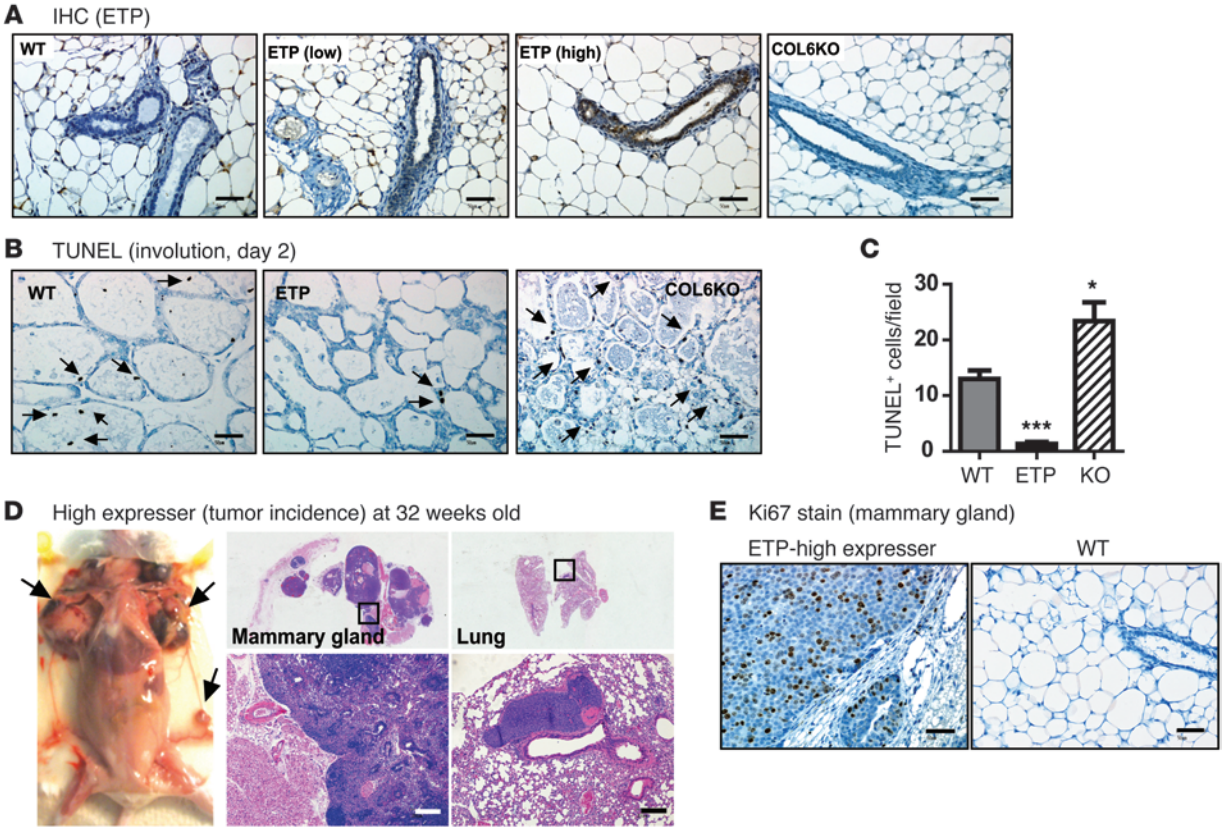

Figure 4

Transgenic mice expressing ETP under the MMTV promoter. (**A**) ETP immunostaining showing strong ETP positive signal in mammary ductal epithelium in the transgenic mice lines (ETP low and high), but not WT and *Col6a1*$^{-/-}$ mice. Scale bars: 50 μm. (**B** and **C**) Antiapoptotic effects of ETP. (**B**) Apoptosis for mammary epithelial cells during involution was determined by TUNEL assay on mammary glands of WT, ETP, and *Col6a1*$^{-/-}$ mice 2 days after forced weaning. Arrows indicate TUNEL-positive apoptotic cells. Scale bars: 50 μm. (**C**) Quantification of TUNEL-positive cells, represented as mean ± SEM (multiple images, $n = 3$ per group). ***$P < 0.001$, *$P < 0.05$ vs. WT, unpaired t test. (**D** and **E**) Promitotic effects of ETP. High ETP expressers (32 weeks old) spontaneously developed tumors. (**D**) Whole body image (left; arrows indicate tumors) and H&E staining of mammary gland (middle) and lung (right) tissue. Boxed regions are shown at higher magnification below. Scale bars: 200 μm. (**E**) Cell proliferation was determined by Ki67 staining with mammary glands of 32-week-old ETP high-expressing and WT mice. Scale bars: 50 μm.

Effects of ETP synergize with the canonical TGF-β pathway to promote lung metastasis. To delineate the mechanism underlying the increase in EMT processes in PyMT/ETP mice, we investigated the effects of ETP on the TGF-β pathway. TGF-β signaling has previously been implicated in EMT-associated tumor growth and metastasis, which are associated with the acquisition of metastatic traits (26). To examine whether ETP signaling converges with the canonical TGF-β pathway, we generated 2 ETP constructs: a form that was secretion incompetent, and thus retained within the secretory pathway, as well as a secreted form (Supplemental Figure 6A). We used these constructs for a reporter assay with TGF-β–dependent Smad protein–binding elements (SBEs) (27). Interestingly, only the secreted form of ETP enhanced SBE reporter activity; furthermore, this was critically dependent on TGF-β stimulation (Figure 7B), which indicates that ETP synergizes with the TGF-β pathway through cell-surface interactions. This is based on the fact that the enhanced TGF-β signaling synergistically activated through ETP was completely abolished by treatment with the monoclonal TGF-β neutralizing antibody 1D11 (Figure 7C), which strongly suggests that ETP-dependent SBE reporter activation and consequent signaling events fully rely on the presence of TGF-β.

To further elucidate the TGF-β–dependent role of ETP as a tumor enhancer, in a less aggressive experimental setting of tumor progression, we used an allograft model in which we inhibited TGF-β signaling with TGF-β neutralizing antibodies in the context of ETP overexpression. Although tumor growth for Met-1 cells was significantly enhanced by ETP, TGF-β inhibition did not efficiently reduce ETP-induced tumor growth (Figure 7D), which suggests that TGF-β–mediated signaling is less relevant for the growth of primary tumors in the ETP-expressing tumor stroma. Histological analysis of tumor tissues revealed an increase in mesenchymal-like stromal cells in the ETP-expressing tumor stroma, a phenomenon that was reversed by TGF-β inhibition (Figure 7E). This further suggests that the TGF-β pathway participates in ETP-induced EMT. Additionally, the ETP-mediated increase in tissue fibrosis was attenuated by TGF-β inhibition (Figure 7F). These results were subsequently confirmed by examining EMT markers in tumor tissues (Figure 7G), namely E-cadherin, vimentin, and α-SMA, which is an activated myofibroblast marker widely used for EMT assessment (6). Of note, manipulation of TGF-β signals in tumor tissues using genetic mouse models for TGF-β, TGF-βR1, and TGF-βRII (28–30) have highlight-

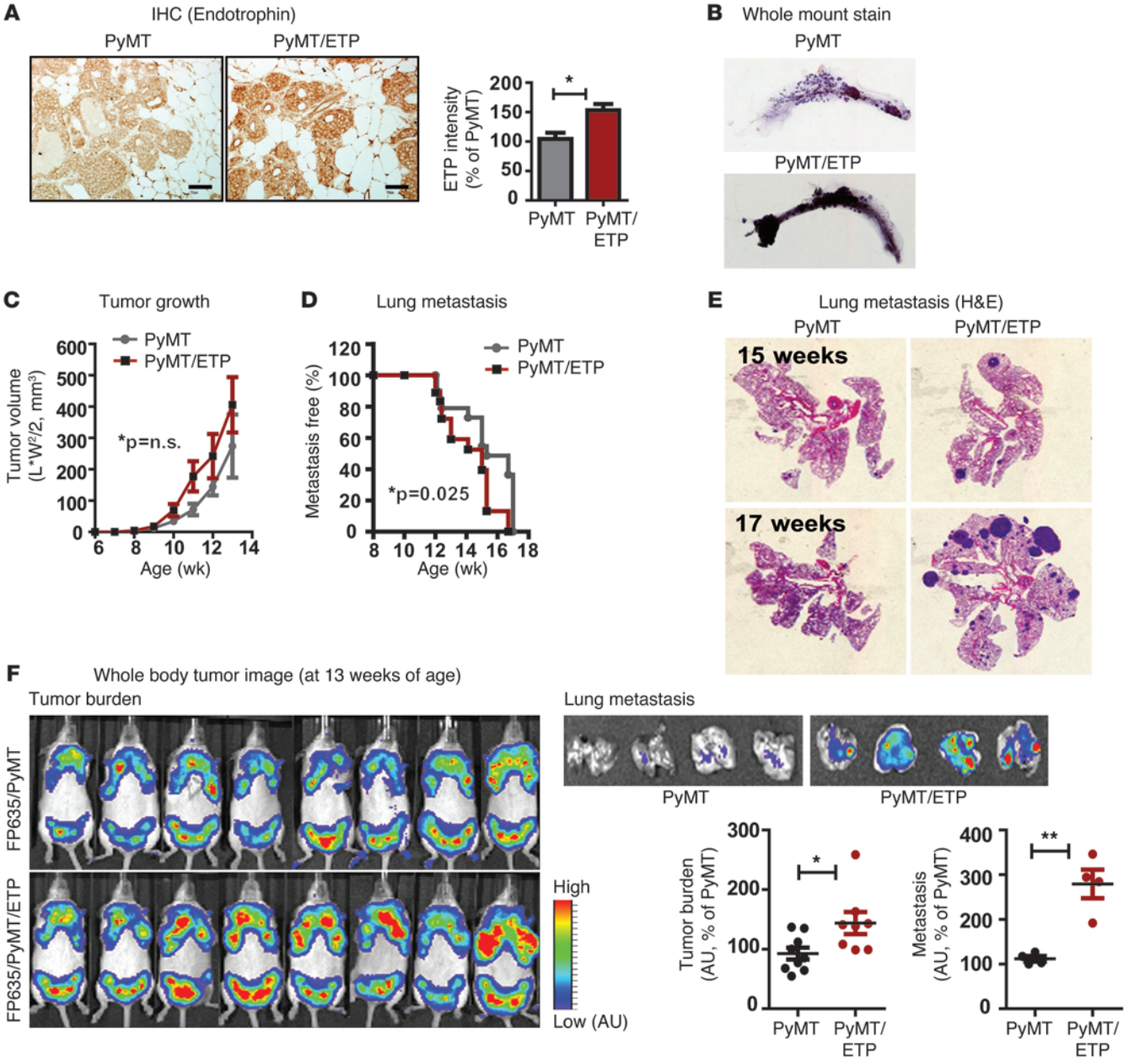

Figure 5

ETP augments primary tumor growth and pulmonary metastasis in the background of PyMT mice. (**A**) ETP immunostaining, with a high ETP-positive signal in tumor tissues from 12-week-old PyMT and PyMT/ETP mice. Scale bars: 50 μm. Intensity of ETP staining was quantified and represented as mean ± SEM (n = 5 per group). *P = 0.02 vs. PyMT, unpaired t test. (**B**) Whole-mount staining of mammary gland tissues from 8-week-old PyMT and PyMT/ETP mice, with early neoplastic lesion areas increased by ETP. (**C**) Tumor volume was determined by weekly caliper measurements from PyMT (n = 35) and PyMT/ETP (n = 38) mice. Results are represented as mean ± SEM. P = NS, 2-way ANOVA. (**D** and **E**) ETP augmented pulmonary metastasis. (**D**) Pulmonary metastatic growth was determined by measuring the tumor incidence in lung tissues (8- to 17-week-old, n = 22–25 per group). H&E-stained preparations for lung tissues were used for analysis. Shown is percent metastasis-free mice over time. *P = 0.025, log-rank test. (**E**) Representative H&E stain for lung tissues showing the degree of pulmonary metastasis in 15- and 17-week-old PyMT and PyMT/ETP mice. (**F**) Representative whole-body images for tumor burden. Tumor volume for 13-week-old FP635/PyMT and FP635/PyMT/ETP mice was monitored by IVIS fluorescence scanner. Metastatic burden was determined by fluorescence signals in lung tissues. Quantified results are represented as mean ± SEM (n = 8–9 per group). *P = 0.0117, **P = 0.0011 vs. PyMT, unpaired t test.

ed that TGF-β signaling augments cancer cell invasiveness, primarily through stimulation of EMT processes, enhancing metastatic rather than primary tumor growth. We subsequently investigated the efficacy of TGF-β neutralizing antibodies on the metastatic potential of cancer cells from PyMT/ETP and PyMT mice (referred to herein as ETP$^+$- and Ctrl-cancer cells, respectively). ETP$^+$-cancer cells metastasized at a higher rate than Ctrl-cancer cells (Figure 7H). Moreover, this increased rate of metastasis was attenuated by TGF-β inhibi-

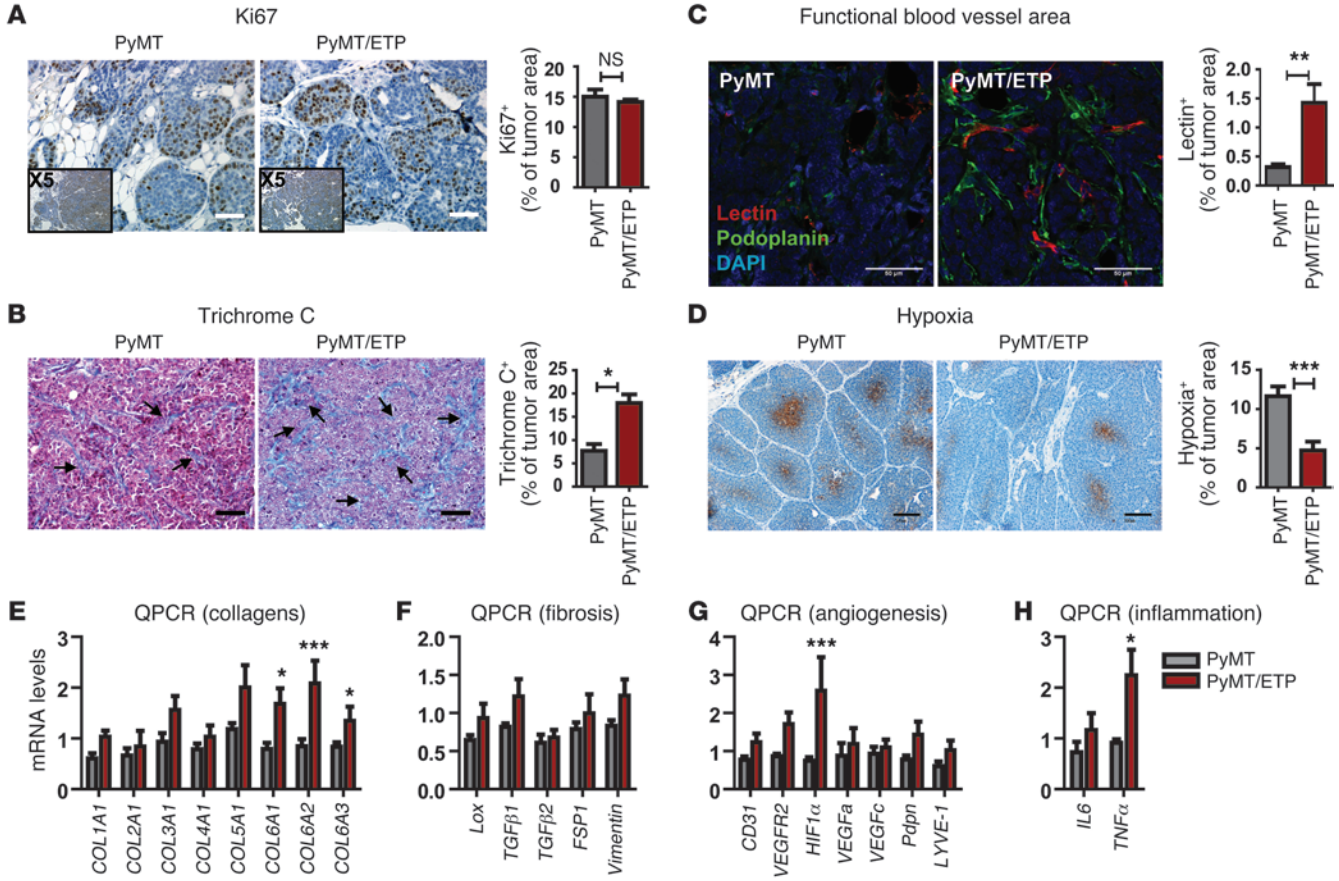

Figure 6

Histological analysis for tumor tissues of PyMT/ETP versus PyMT mice. (**A**) Proliferation indices were determined by immunostaining with Ki67. Quantified results represent mean ± SEM (n = 5 per group). P = NS vs. PyMT, unpaired t test. (**B**) Fibrosis indices were determined by Masson's Trichrome C stain. Percent fibrotic area over the tumor lesions was quantified. Data represent mean ± SEM (n = 5 per group). $^{**}P$ = 0.01 vs. PyMT, unpaired t test. Arrows indicate collagen fibrils. (**C**) Functional blood vessel areas were determined by lectin perfusion. Podoplanin (lymphangiogenesis marker) and DAPI (nucleus) were costained. Quantified results represent mean ± SEM (n = 5 per group). $^{**}P$ = 0.003 vs. PyMT, unpaired t test. (**D**) Hypoxia was determined by pimonidazole-HCl injection. Hypoxic lesions were stained in dark brown. Quantified results represent mean ± SEM (n = 5 per group). $^{***}P$ = 0.0007 vs. PyMT, unpaired t test. (**E**–**H**) Total RNA was prepared from the tumor tissues from PyMT/ETP and PyMT mice. mRNA levels for the genes responsible for fibrosis and EMT (**E** and **F**), angiogenesis and lymphangiogenesis (**G**), and inflammation (**H**) were determined by qRT-PCR. mRNA levels were normalized with β-actin and represented as mean ± SEM (n = 8 per group). Relative values of each gene are represented as fold change relative to PyMT. $^{*}P < 0.05$, $^{***}P < 0.001$ vs. PyMT, 2-way ANOVA. Scale bars: 50 μm (**A**–**C**); 100 μm (**D**). Insets in **A** are enlarged ×5.

tion (Figure 7H). Collectively, these results suggest that the TGF-β–dependent aspects of ETP action relate only to the acquisition of cancer cell invasive and metastatic traits, not to primary tumor growth.

Reconstitution of ETP into Col6a1$^{-/-}$-cancer cells augments tumor growth, with higher tissue fibrosis and EMT. We determined that Met-1 cells did not grow in a *Col6a1*$^{-/-}$ host (Figure 1). Furthermore, allografts of *Col6a1*$^{-/-}$-cancer cells (isolated from tumor tissues of PyMT/*Col6a1*$^{-/-}$ mice) implanted into isogenic WT mice failed to thrive (Figure 8A). To determine whether ETP can restore the blunted tumor growth of *Col6a1*$^{-/-}$-cancer cells, the growth rate of *Col6a1*$^{-/-}$/ETP cells (isolated from PyMT/*Col6a1*$^{-/-}$/ETP mice, in which ETP was reconstituted into the PyMT/*Col6a1*$^{-/-}$ background) was analyzed and compared with Ctrl- or *Col6a1*$^{-/-}$-cancer cells. Tumor growth and tumor weight were significantly increased with *Col6a1*$^{-/-}$/ETP versus *Col6a1*$^{-/-}$ cells (Figure 8, A–C). Even though ETP reconstitution rescued tumor growth of *Col6a1*$^{-/-}$-cancer cells, tumors remained smaller in size than those obtained with Ctrl-cancer cells (Figure 8, A–C). This suggests that ETP alone is not sufficient to completely reconstitute growth of *Col6a1*$^{-/-}$-cancer cells. However, a number of important aspects were reproduced with ETP reconstitution. Significant ETP-induced changes in *Col6a1*$^{-/-}$-cancer cells included tissue fibrosis as well as an enhanced EMT process (Figure 8, D–G). Notably, the FSP-1^{+} fibroblast population was not responsive to ETP (Figure 8H), which suggests that the ETP response is cell type specific.

ETP, as a potent chemokine, augments primary tumor growth through tumor-stromal interactions. To examine cancer cell–autonomous effects, we performed allografts without Matrigel plugs. Tumor growth of ETP^{+}-cancer cells was comparable to Ctrl-cancer cells (Supplemental Figure 7A). Indeed, in vitro examination of mammary cancer cells, including Met-1 and MCF-7 cells, revealed that cell proliferation was not affected by addition of purified ETP (Supplemental Figure 7, B

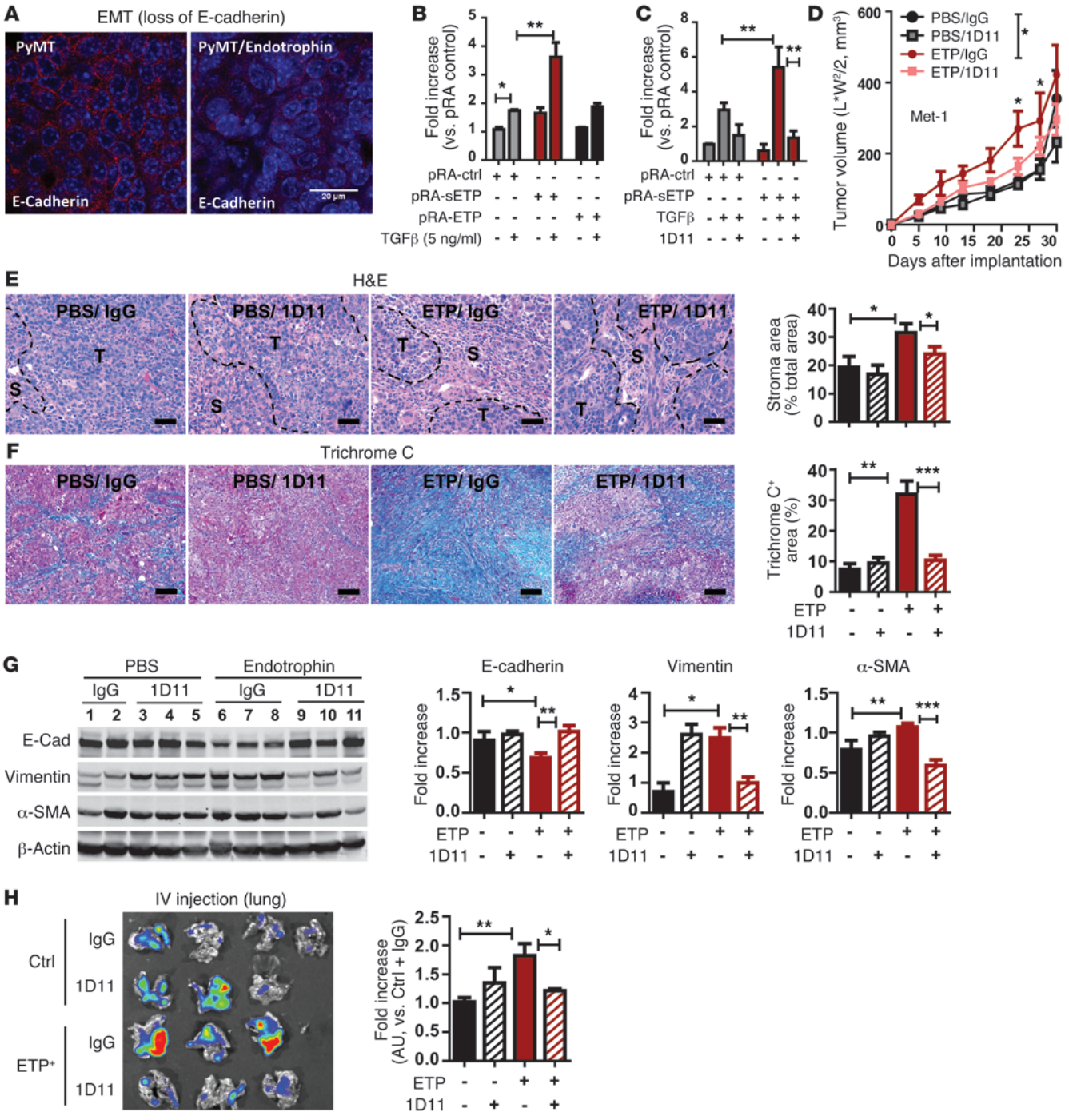

Figure 7

ETP augments metastasis through enforcing TGF-β–dependent EMT. (**A**) E-cadherin immunostaining for tumor tissues from PyMT and PyMT/ETP. (**B** and **C**) SBE-luciferase reporter assay. See Supplemental Methods for details. Data represent fold increase (3 independent experiments). $^{**}P < 0.01$, $^{*}P < 0.05$, 2-way ANOVA. pRA-ctrl, empty; pRA-sETP, secretion form; pRA-ETP, intracellular form. (**D**–**G**) Allografts of Met-1 cells in the presence of either ETP (20 ng/plug) or PBS mixed with 1D11 or IgG (10 μg/plug) within a Matrigel plug. 10 days after implantation, additional 1D11 or IgG (100 μg) was i.p. injected once a week during tumor progression. (**D**) Tumor volumes represent means ± SEM ($n = 5$ per group). $^{*}P < 0.05$, 2-way ANOVA. (**E**) H&E staining. The ratio of stromal area in tumor tissues was quantified. Data represent mean ± SEM ($n = 5$ per group). $^{*}P < 0.05$, unpaired *t* test. T; tumor and S; stroma. (**F**) Fibrosis was determined by Masson's Trichrome C stain. Data represent mean ± SEM ($n = 5$ per group). $^{**}P < 0.01$, $^{***}P < 0.001$, unpaired *t* test. (**G**) Western blotting for EMT markers E-cadherin, vimentin, and α-SMA. β-actin, loading control. Data represent fold increase ($n = 5$ per group). $^{*}P < 0.05$, $^{**}P < 0.01$, $^{***}P < 0.001$, unpaired *t* test. (**H**) Control and ETP⁺-cancer cells were isolated from FP635/PyMT and FP635/PyMT/ETP mice and conveyed into WT mice by tail vein injection (0.5×10^6 cells/mouse). Either IgG or 1D11 (100 μg) was i.p. injected every 5 days. 20 days post injection, metastasized cancer cells in the lung tissues were determined by fluorescence intensity. Data represent fold increase ($n = 3$–4 per group). $^{**}P < 0.01$, $^{*}P < 0.05$, unpaired *t* test. Scale bars: 20 μm (**A**); 50 μm (**E**); 100 μm (**F**).

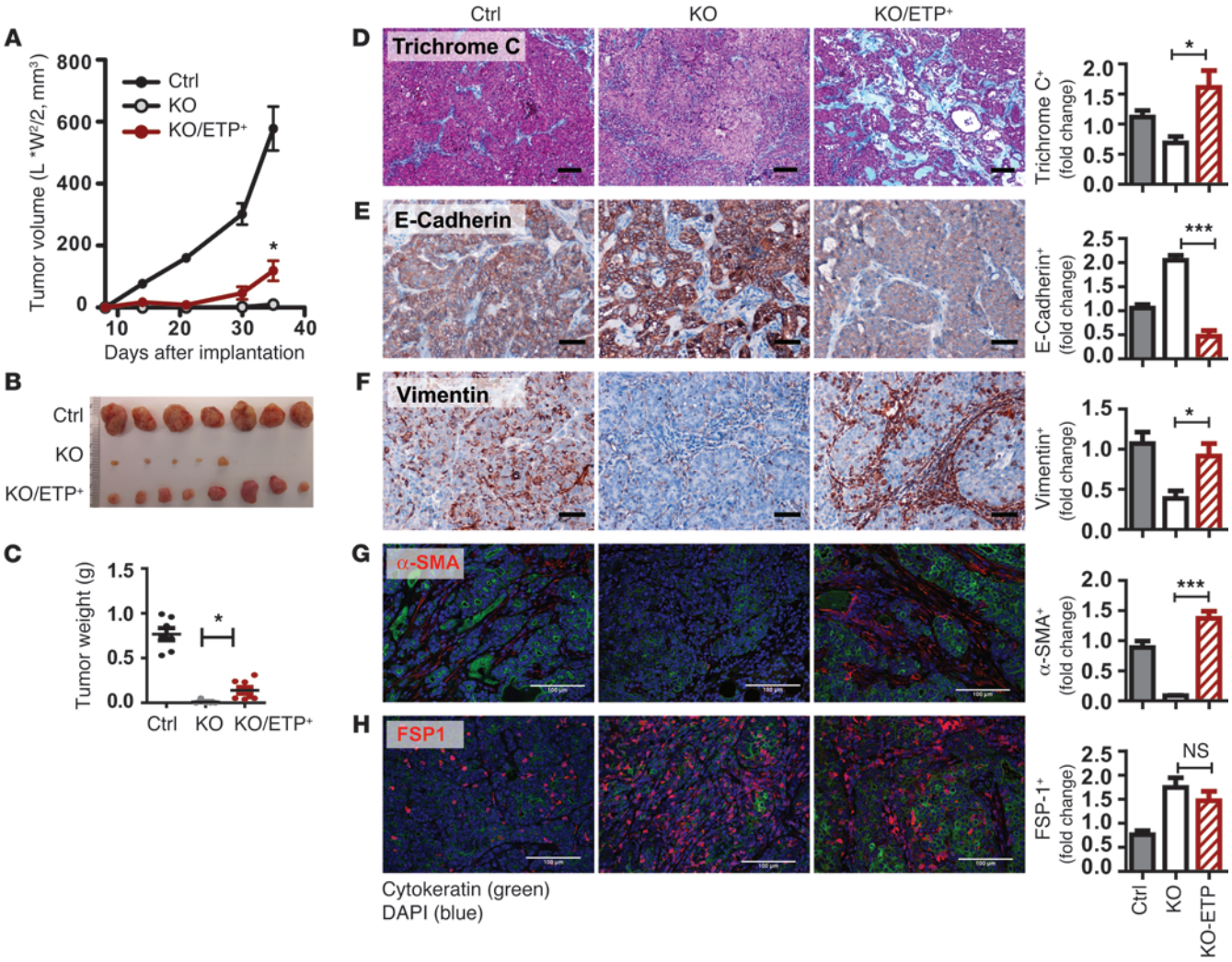

Figure 8

ETP reconstitution into *Col6a1*$^{-/-}$-cancer cells rescues tumor growth. Cancer cells isolated from PyMT, PyMT/*Col6a1*$^{-/-}$, and PyMT/*Col6a1*$^{-/-}$/ETP mice were mixed with the same volume of Matrigel (50 μl) and implanted into WT mice (0.5 × 10^6 cells/mouse). (**A**) Tumor growth (mean ± SEM; n = 5–8 per group), determined by caliper measurements. *P = 0.024 vs. *Col6a1*$^{-/-}$, unpaired t test. (**B**) Representative image 35 days after implantation. (**C**) Tumor weight (mean ± SEM; n = 5–8 per group). *P = 0.023 vs. *Col6a1*$^{-/-}$, unpaired t test. (**D**–**H**) Tissue fibrosis was determined by Masson's Trichrome C stain (**D**), and EMT was determined by immunostaining for E-cadherin (**E**), vimentin (**F**), α-SMA (**G**), and FSP-1 (**H**). Cytokeratin (epithelial cells) and DAPI (nucleus) were costained in **G** and **H**. Positive staining areas were quantified and represented as fold increase over Ctrl-tumors (multiple images, n = 5 per group). *P < 0.05, ***P < 0.001 vs. *Col6a1*$^{-/-}$, unpaired t test. Scale bars: 50 μm (**E** and **F**); 100 μm (**D**, **G**, and **H**).

and C). However, the vascularization of allografts of ETP$^+$-cancer cells was significantly increased (Supplemental Figure 7D). This suggests that cancer cells per se are not responsive to ETP with respect to growth, but that ETP augments endothelium formation; therefore, tumor stromal, rather than cancer cell–autonomous, interactions account for the increase in tumor growth observed in vivo. To test this, ETP$^+$- and Ctrl-tumors were implanted into isogenic WT mice. ETP$^+$-tumors grew dramatically faster than did Ctrl-tumors (Figure 9A). From these allograft studies, the potent proangiogenic, profibrotic, and proinflammatory effects of ETP, initially observed in the PyMT setting (Figure 6), became evident (Supplemental Figure 8). In light of this, we focused on stromal effects on primary tumor growth. These stromal effects were mediated by the tumor-associated vasculature, as well as fibrotic and inflammatory pathways. Major stromal target cell types involved in tumor interactions were endothelial cells, fibroblasts, and macrophages, all of which have established roles in tumor growth and metastasis (31).

In light of the findings above, we hypothesized that ETP functions as a chemokine during tumor stroma expansion, recruiting or possibly activating stromal cells to support tumor growth. In vivo targeted cell recruitment studies revealed that Matrigel plugs combined with recombinant ETP and injected into mammary fat pads of WT mice recruited significantly more stromal cells than did PBS (Figure 9B). We subsequently generated monoclonal anti-ETP antibodies to effectively neutralize ETP, thereby generating an ETP-based therapeutic approach

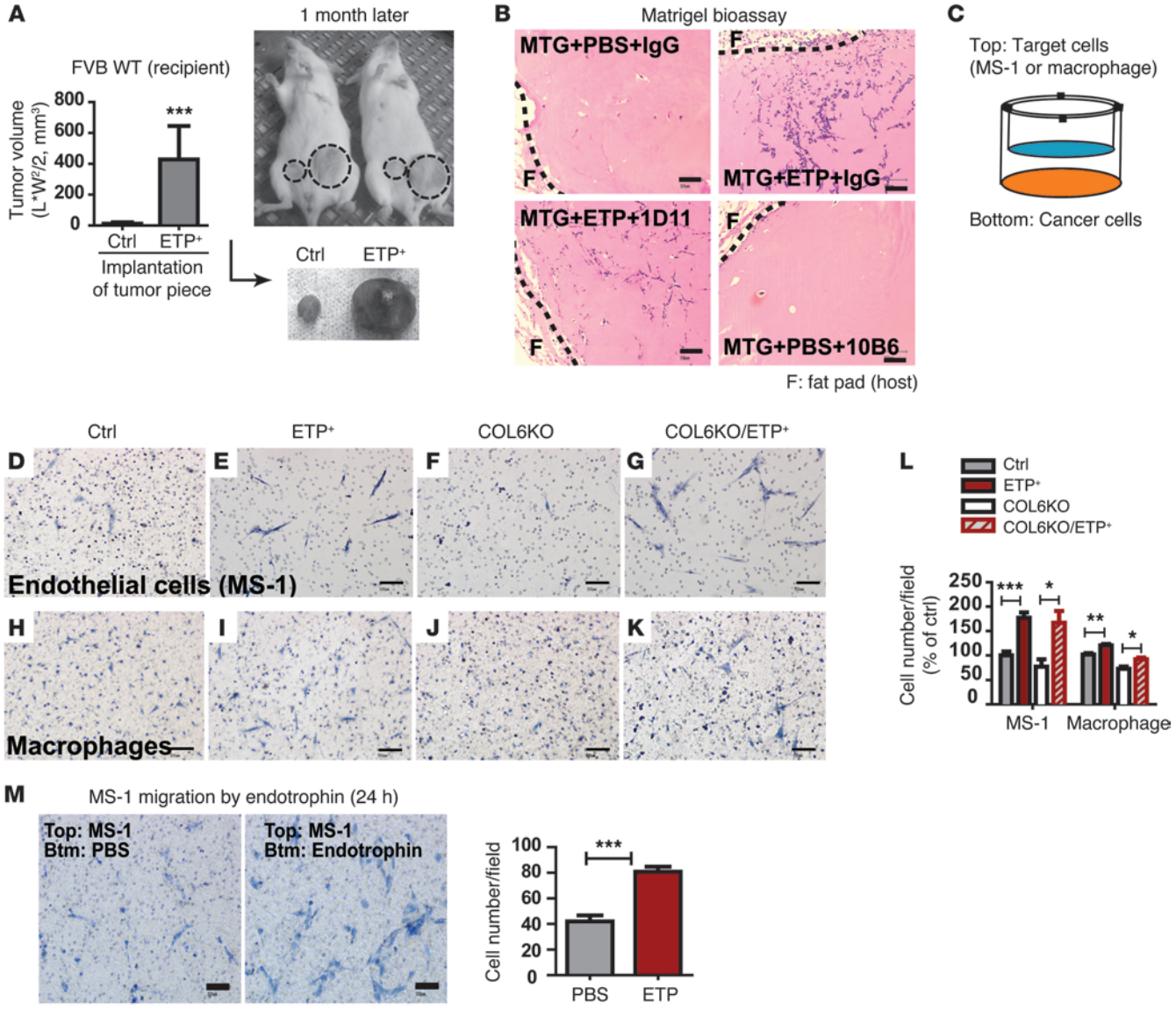

Figure 9

ETP acts as a chemokine augmenting tumor growth. (**A**) Tumor growth significantly increased in ETP$^+$-tumor tissue allograft into WT mice. Tumor volume was determined 1 month after implantation (representative images). Data represent mean ± SEM (n = 5 per group). ***P < 0.001, unpaired t test. (**B**) In vivo Matrigel bioassay. Matrigel (50 μl) was mixed with ETP (100 ng/plug) or PBS and implanted into WT mice in the presence of IgG, 1D11, or 10B6 (20 μg/plug). 2 days after implantation, plugs were excised and stained for H&E. Scale bars: 100 μm. (**C**–**L**) Cancer cells were plated in the bottom chamber 1 day prior to seeding MS-1 cells (5 × 10^5 cells/well) and macrophages (1 × 10^5 cells/well) atop the membrane chamber in Transwell and incubated for 18–24 hours (**C**). (**D**–**K**) Representative images of multiple independent experiments. Scale bars: 100 μm. (**L**) Quantitation (mean ± SEM; n = 3 per group). ***P < 0.001, **P < 0.05, *P < 0.01, unpaired t test. (**M**) MS-1 migration assay. MS-1 cells (5 × 10^5 cells/well) were plated atop the chamber in Transwell and incubated for 24 hours. Chemotaxis was set up by following cell migration from DMEM/serum-free to DMEM/2% FBS/PBS or DMEM/2% FBS/ETP protein (1 μg/well). Images are representative of multiple independent experiments. Data represent mean ± SEM (n = 3 per group). ***P = 0.008, unpaired t test. Scale bars: 100 μm.

(Supplemental Figure 1C). Chemokine activity of ETP was completely blocked by 10B6, but not by 1D11 (Figure 9B), which suggests that ETP-inherent chemokine activity was independent of TGF-β signaling. Furthermore, the majority of cells recruited into the Matrigel plugs by ETP were CD31$^+$ endothelial cells (Supplemental Figure 9A). Similarly, we analyzed primary mammary epithelial cancer cells isolated from tumor tissues of PyMT, PyMT/ETP, PyMT/*Col6a1*$^{-/-}$, and PyMT/*Col6a1*$^{-/-}$/ETP mice for their chemoattractive potential. More specifically, mammary epithelial cancer cells were cocultured with either mouse endothelial cells (MS-1; Figure 9, D–G) or primary macrophages (Figure 9, H–K) in a Transwell plate (Figure 9C), and the migration of the MS-1 cells and macrophages were subsequently quantified (Figure 9L). ETP$^+$-cancer cells recruited substantially

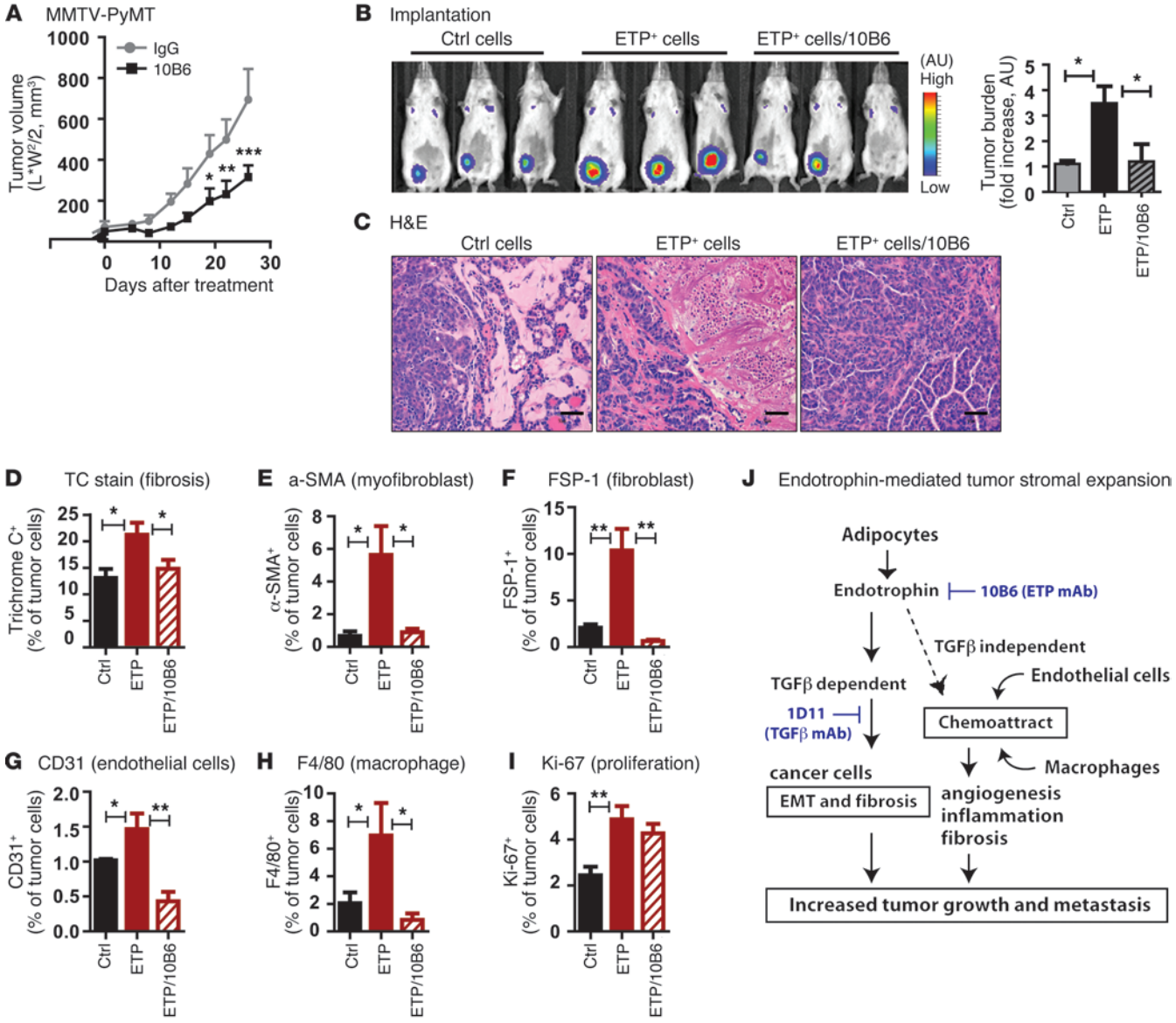

Figure 10

10B6 blocks ETP-mediated stromal expansion in vivo. (**A**) 10B6 (200 μg/mouse) was i.p. injected twice weekly into PyMT mice from 9 to 13 weeks of age. Tumor growth (mean ± SEM; n = 4–6 per group) was determined by weekly caliper measurements. *P < 0.05, **P < 0.01, ***P < 0.001 vs. IgG control, 2-way ANOVA. (**B**) Primary mammary epithelial cancer cells were isolated from 12-week-old FP635/PyMT and FP635/PyMT/ETP mice and implanted into WT recipients with the same volume of Matrigel. For the 10B6 group, 10B6 was added in a Matrigel plug (10 μg/plug) admixed with ETP⁺-cancer cells (i.e., ETP⁺/10B6). A representative whole-body image was acquired 25 days after implantation using IVIS fluorescence scanner. Artificial color indicates fluorescence signal intensity accounts for tumor volume (AU). Quantitative results are represented as mean ± SEM (n = 3 per group). *P < 0.05, unpaired t test. (**C**–**I**) 6 weeks after implantation, tumor tissues were excised from Ctrl-, ETP⁺-, and ETP⁺/10B6-cancer cells allografted mice and stained for H&E (**C**), Masson's Trichrome C (**D**), α-SMA (**E**), FSP-1 (**F**), CD31 (**G**), F4/80 (**H**), and Ki67 (**I**). Quantified results in **D**–**I** are mean ± SEM (multiple images, n = 3 per group). *P < 0.05, **P < 0.01, unpaired t test. Scale bars: 50 μm. (**J**) Working model for ETP in mammary tumor progression.

more endothelial cells and macrophages (Figure 9, E, I, and L). This effect was not observed in *Col6a1*$^{-/-}$-cancer cells (Figure 9, F, J and L). More importantly, ETP reconstitution into *Col6a1*$^{-/-}$-cancer cells completely recovered their chemoattractant properties (Figure 9, G, K, and L), to a level comparable with ETP⁺-cancer cells. This suggests that the majority of chemoattractant properties exerted by COL6 are exerted by ETP.

In vitro cell migration assays revealed that ETP recruited twice as many MS-1 cells than did controls (Figure 9M). Furthermore, in vitro angiogenesis assays using MS-1 cells demonstrated that endothelial cells incubated with conditioned media from ETP-overexpressing HEK-293T cells mobilized and organized vasculature structures much more actively than conditioned medium harvested from control HEK-293T cells (Supplemental Figure

9B). 10B6 completely blocked these effects (Supplemental Figure 9B). Thus, ETP plays a crucial role in endothelial cell recruitment, migration, and vessel formation during the process of angiogenesis. Based on these observations, we conclude that ETP is critical for the recruitment of stromal cells into the tumor microenvironment through its action as a chemokine.

A neutralizing anti-ETP monoclonal antibody attenuates tumor growth by inhibiting ETP-mediated expansion of the tumor stroma. We next examined whether ETP neutralization can attenuate tumor progression. Of note, PyMT mice expressed high levels of endogenous ETP in the tumor-infiltrated stromal compartment (Figure 2E). Tumor growth was significantly attenuated by 10B6 treatment compared with isotype control IgG treatment (Figure 10A). Similarly, FP635/ETP$^+$-cancer cells were implanted into WT mice, with or without 10B6 added to the Matrigel plug; tumor growth was then monitored using fluorescence imaging. The rate of ETP$^+$-cancer cell growth was significantly higher relative to Ctrl-cancer cells; however, their growth was effectively attenuated by 10B6 (Figure 10B). Histological analysis of tumor tissues indicated that various stromal cells had the capacity to infiltrate into the Matrigel plugs containing ETP$^+$-cancer cells. Again, 10B6 inhibited ETP-mediated tumor stromal expansion and eventually triggered tumor regression (Figure 10C). ETP$^+$-cancer cell allografts consistently displayed higher levels of fibrosis (Figure 10D) and a high degree of stromal cell infiltration, including by α-SMA$^+$ cells, FSP-1$^+$ fibroblasts, and CD31$^+$ endothelial cells in addition to F4/80$^+$ macrophages (Figure 10, E–H). These cells were highly proliferative, as demonstrated by Ki67$^+$ staining (Figure 10I). As expected, the ETP-mediated increase in fibrosis and stromal expansion was completely blocked by 10B6 (Figure 10, D–H). Collectively, our results indicated that stromal adipocytes play a crucial role in mammary tumor progression; that ETP is a powerful stromal factor that exerts a major influence on primary tumors through its chemokine activities; and that ETP can affect metastatic growth via TGF-β–mediated EMT. Thus, ETP-directed approaches may serve as novel therapeutic regimens in the treatment of breast cancer (Figure 10J).

Discussion

A prominent environmental stimulus of tumor dissemination is hypoxia, triggered by a high demand for cell proliferation and insufficient angiogenesis. Comparable to this process, hypertrophic AT expansion during obesity can also trigger local hypoxia (32) that can further progress to AT fibrosis (33). These obesity-related pathophysiological changes can lead to an environment that is conducive to cancer growth, such as chronic inflammation, inadequate angiogenesis, and enhanced fibrosis (8). In this setting, obesity may contribute to an ETP-rich tumor microenvironment through a positive feed-forward mechanism. Indeed, COL6α3 message levels are upregulated in obese AT (34). COL6 upregulation has been reported in various aspects of tumor progression. Malignant cancer cells can also express COL6; this has been reported for the mammary gland (18), the colon (35, 36), pancreatic ductal adenocarcinomas (37), and hepatocarcinomas (38). Thus, the source of ETP in the tumor microenvironment may be heterogeneous, with signals cooperatively influencing cancer cell behavior through paracrine and autocrine pathways. Nevertheless, stromal adipocytes represent a prominent source for COL6 in the mammary tumor microenvironment (Supplemental Figure 10A). However, the detailed mechanisms underlying the specific effects of COL6 on tumor behavior have not fully been elucidated. Here, we have highlighted that ETP, a cleaved product of COL6, is likely to be a critical mediator of several tumor-associated phenomena and is of particular importance in tumor progression in the context of obesity.

Within the tumor milieu, EMT is initiated by extracellular stimuli. This can be exerted by ECM components (collagens, fibronectin, hyaluronic acids, and MMPs) as well as by certain growth factors (TGF-β, EGF, and HGF), all of which are provided by both paracrine and autocrine signals within the tumor microenvironment (25). One of the prominent ECM molecules released from stromal adipocytes is COL6. As a COL6 processing product, ETP plays an important role in the local microenvironment, stimulating TGF-β–dependent EMT in the context of mammary tumors to potentiate prometastatic effects (Figure 7). Gene expression profiling and immunostaining of tumor tissues from PyMT/ETP mice confirmed enhanced ETP-mediated acquisition of EMT characteristics, whereas in vitro data indicated that ETP alone did not induce EMT (data not shown). This suggests that ETP may function as an important costimulator of existing pathways for the EMT, such as TGF-β signaling and possibly activation of integrins and Wnt signals.

Increased tissue fibrosis, combined with high tissue rigidity (due to ECM remodeling and crosslinking), is positively associated with tumor growth (39). Our results revealed an ETP-induced fibrotic environment, with high levels of myofibroblast accumulation within tumor tissues, as a key characteristic of ETP action. These activated myofibroblasts in ETP$^+$-tumors were derived, at least in part, by EMT. However, we cannot rule out that ETP may facilitate additional processes, such as microfibril assembly of preexisting collagen fibers (15) or stimulation of myofibroblast differentiation (40). Moreover, promoting transformed mesenchymal cell proliferation can enhance the appearance of additional stromal cells (41); ETP may also effectively promote this process. Indeed, blocking the EMT by using a TGF-β neutralizing antibody did not completely eliminate fibrosis in ETP$^+$-tumors (Figure 7F). These data indicate that the ETP-induced EMT and subsequent fibrotic traits in tumors contribute to an increase in tumor growth and metastasis, which highlights a central role for ETP in tumor progression.

We have also provided evidence for the potent ETP-mediated chemoattractant properties. These ETP effects can even be mimicked in a tumor-free environment. A number of reports highlight significant correlations between COL6α3 and chronic inflammation, based on increased macrophage infiltration into AT depots of obese subjects (42, 43). We propose that the ETP-mediated chemoattractant properties described herein may offer a mechanistic basis for these clinical correlations. Neutralizing these ETP-mediated effects in normal, tumor-free AT may yield beneficial outcomes as well. Our current efforts are directed toward adipocyte-derived overexpression of ETP, which will answer the question of whether a local excess of ETP will exert beneficial effects (due to its proangiogenic properties) or negative effects (due to its proinflammatory and profibrotic properties) on a fat pad not challenged with an invading tumor.

We have limited insights into the stepwise process that leads to cleavage of ETP from its parent molecule. We do not know which proteases are involved, or from where they originate. Fibrosis in obese AT is associated with an increase of various MMPs or TIMPs resulting in collagen degradation (44). MMP-11, MMP-2, and MMP-9 have been suggested as peptidase for COL6 (45, 46),

although there is no further evidence whether these MMPs cleave ETP. Base on the fact that most cancer cells express high levels of MMPs associated with tumor growth and metastasis (47), it is likely that there are abundant sources for ETP cleavage activity within the tumor microenvironment. The identification of the critical protease involved in ETP processing may offer a new approach to curbing growth by pharmacologically inhibiting this step. Our findings unveiled an important role of the adipocyte as an active component of the tumor stroma that actively interacts with cancer cells and a number of other relevant local cell types. Our data highlight that an adipocyte-derived ECM cleavage product actively contributed toward the remodeling of the tumor microenvironment by enabling the progression of tumor growth and metastasis through enhancement of the EMT process and subsequent chemotaxis of endothelial cells and macrophages. In many aspects, the deposition of ECM components, such as ETP in the tumor stroma, resembles a wound-healing process, as this involves the recruitment and stimulation of immune cells, endothelial cells, and fibroblasts during the wound repair process. However, unlike during the wound-healing process, ETP prompts cancer cells to sustain mesenchymal cell–like traits and activates fibroblasts in the tumor stroma, drastically increasing local fibrosis and eventually enhancing metastatic growth. Our findings have further implications for several tissues that have an associated pathological fibrotic component, such as the liver (48), cartilage (49), lung (50), and heart (51); COL6 expression has been documented in all these tissues. Future efforts targeted toward ETP neutralization in various pathological settings should establish whether this approach is a viable antifibrotic strategy that is generally beneficial, not only in the setting of tumor progression and metastasis, but also during normal AT expansion.

Methods

See Supplemental Methods and complete unedited blots in the supplemental material.

Mice. See Supplemental Methods for detailed information on the mice used herein. All experiments were conducted using littermate-controlled female mice. All animals used in this study were in a pure FVB background.

Tumor imaging. FP635/PyMT mice or cancer cells isolated from tumors from FP635/PyMT mice were imaged with an IVIS scanner (Caliper Lifesciences), and the signal intensity was analyzed with Living Image version 3.2 (Caliper Lifesciences). See Supplemental Methods for conventional analyses of tumor growth and metastasis.

ETP-specific polyclonal and monoclonal antibodies. ETP-GST fusion proteins for both mouse and human ETPs were purified from bacteria and used as antigens for polyclonal antibodies (Covance). For monoclonal antibody generation, native ETP was purified by gel filtration chromatography (GE Healthcare) from conditioned media of a mouse ETP-overexpressing HEK-293 stable cell line. See Figure 2A for ETP amino acid sequences.

Quantitative RT-PCR. Total RNA was isolated using the RNeasy kit (Qiagen) following tissue homogenization in TRIzol (Invitrogen). Total RNA (1 μg) was reverse transcribed with SuperScript III reverse transcriptase (Invitrogen). Quantitative real-time PCR (qRT-PCR) was performed using Roche Lightcycler 480. Primer sequences used in this study have been described previously (33, 34, 52).

Analysis of ETP homing. The homing of ETP in circulation was determined by injecting fluorescently labeled ETP into tail veins. ETP and IgGs were labeled with IRDye800 CW NHS Ester (Licor Bioscience) at a 1:1 molar ratio (dye/protein), according to the manufacturer's instructions. Whole-body fluorescence images were collected on the Odyssey scanner (Licor Bioscience). All scans were performed under anesthesia (Aerrane) using an EZ-2000 Microflex small-animal anesthesia system (EZ Systems). At the end of experiments, each organ was collected and imaged for signal intensity with the Odyssey scanner. Quantified values were normalized to the total area of each organ.

Histological analysis. Formalin-fixed paraffin-embedded tissue sections were used for immunohistochemistry. Deparaffinized tissue slides were stained with the primary antibodies shown in Supplemental Methods. Staining for functional blood vessels and hypoxic lesions as well as whole-mount staining of mammary glands were followed as described previously (52). TUNEL assays were performed according to the manufacturer's protocol (Trevigen Inc.). Masson's Trichrome C and H&E staining were performed by J. Shelton (University of Texas Southwestern Medical Center, Dallas, Texas, USA). Deidentified human tumor samples were obtained from the University of Texas Southwestern Tissue Resource.

Primary culture of mammary cancer cells and implantation. Isolation of mammary epithelial cancer cells and implantation procedures were as previously described (52). Tumor growth was monitored once weekly beginning 2 weeks after implantation.

In vitro cell migration assay. Thioglycollate-elicited macrophages or MS-1 in serum-free media were loaded into the upper chamber of a Transwell plate (8 μm pore size; Costar). As chemoattractants, ETP or the indicated cancer cells were added to the bottom chamber with DMEM containing 2% FBS. 18 hours later, cells on the underside of the membrane were fixed with 10% formalin, stained with hematoxylin, and counted. Images were acquired using the Nikon Cool Scope (Nikon).

Statistics. Data are presented as mean ± SEM. Data were analyzed by 2-way ANOVA followed by Newman-Keuls multiple comparison test or by 2-tailed Student's *t* test, as appropriate, with GraphPad Prism version 5 software. A *P* value less than 0.05 was considered statistically significant.

Study approval. This study was carried out in strict accordance with the recommendations of the NIH *Guide for the Care and Use of Laboratory Animals*. All animal experiments were approved by the Institutional Animal Care and Research Advisory Committee at the University of Texas Southwestern Medical Center (protocol no. 2010-0006). All efforts were made to minimize animal suffering.

Acknowledgments

The authors thank the DNA Microarray Core, the Small Animal Imaging resource, and the Transgenic Mouse Core (under the direction of Robert Hammer) at the University of Texas Southwestern Medical Center. We thank Jie Song, Yukiko Mayauchi, and Steven Connell for technical assistance; Christine Kusminski for editorial help; Kai Sun for experimental advice; and the rest of the Scherer, Unger, and Clegg laboratories for helpful discussions. The authors were supported by NIH grants R01-DK55758, R01-CA112023, and P01-DK088761 (to P.E. Scherer) and DK081182 (to J. Horton). J. Park is supported in part by a fellowship from the Department of Defense (USAMRMC BC085909). This study was also supported in part by NCI U24 CA126608, the Harold C. Simmons Cancer Center through NCI Cancer Center Support Grant 1P30 CA142543-01, and the Department of Radiology. The Caliper IVIS Spectrum used in these studies was purchased under NIH grant 1S10RR024757.

Received for publication March 20, 2012, and accepted in revised form August 2, 2012.

Address correspondence to: Philipp E. Scherer, Touchstone Diabetes Center, Department of Internal Medicine, University of Texas Southwestern Medical Center, 5323 Harry Hines Blvd., Dallas, Texas 75390-8549, USA. Phone: 214.648.8715; Fax: 214.648.8720; E-mail: Philipp.Scherer@utsouthwestern.edu.

1. Calle EE, Kaaks R. Overweight, obesity and cancer: epidemiological evidence and proposed mechanisms. *Nat Rev Cancer*. 2004;4(8):579–591.
2. Renehan AG, Tyson M, Egger M, Heller RF, Zwahlen M. Body-mass index and incidence of cancer: a systematic review and meta-analysis of prospective observational studies. *Lancet*. 2008; 371(9612):569–578.
3. Wiseman BS, Werb Z. Stromal effects on mammary gland development and breast cancer. *Science*. 2002;296(5570):1046–1049.
4. Elenbaas B, Weinberg RA. Heterotypic signaling between epithelial tumor cells and fibroblasts in carcinoma formation. *Exp Cell Res*. 2001;264(1):169–184.
5. Pollard JW. Trophic macrophages in development and disease. *Nat Rev Immunol*. 2009;9(4):259–270.
6. Kalluri R, Zeisberg M. Fibroblasts in cancer. *Nat Rev Cancer*. 2006;6(5):392–401.
7. Bergers G, Benjamin LE. Tumorigenesis and the angiogenic switch. *Nat Rev Cancer*. 2003;3(6):401–410.
8. Park J, Euhus DM, Scherer PE. Paracrine and endocrine effects of adipose tissue on cancer development and progression. *Endocr Rev*. 2011;32(4):550–570.
9. Scherer PE. Adipose tissue: from lipid storage compartment to endocrine organ. *Diabetes*. 2006;55(6):1537–1545.
10. Tilg H, Moschen AR. Adipocytokines: mediators linking adipose tissue, inflammation and immunity. *Nat Rev Immunol*. 2006;6(10):772–783.
11. Irish JM, Kotecha N, Nolan GP. Mapping normal and cancer cell signalling networks: towards single-cell proteomics. *Nat Rev Cancer*. 2006; 6(2):146–155.
12. Scherer PE, Bickel PE, Kotler M, Lodish HF. Cloning of cell-specific secreted and surface proteins by subtractive antibody screening. *Nat Biotechnol*. 1998;16(6):581–586.
13. Baldock C, Sherratt MJ, Shuttleworth CA, Kielty CM. The supramolecular organization of collagen VI microfibrils. *J Mol Biol*. 2003;330(2):297–307.
14. Aigner T, Hambach L, Soder S, Schlotzer-Schrehardt U, Poschl E. The C5 domain of Col6A3 is cleaved off from the Col6 fibrils immediately after secretion. *Biochem Biophys Res Commun*. 2002; 290(2):743–748.
15. Lamande SR, Morgelin M, Adams NE, Selan C, Allen JM. The C5 domain of the collagen VI alpha3(VI) chain is critical for extracellular microfibril formation and is present in the extracellular matrix of cultured cells. *J Biol Chem*. 2006;281(24):16607–16614.
16. Iyengar P, et al. Adipocyte-secreted factors synergistically promote mammary tumorigenesis through induction of anti-apoptotic transcriptional programs and proto-oncogene stabilization. *Oncogene*. 2003;22(41):6408–6423.
17. Guy CT, Cardiff RD, Muller WJ. Induction of mammary tumors by expression of polyomavirus middle T oncogene: a transgenic mouse model for metastatic disease. *Mol Cell Biol*. 1992;12(3):954–961.
18. Iyengar P, et al. Adipocyte-derived collagen VI affects early mammary tumor progression in vivo, demonstrating a critical interaction in the tumor/stroma microenvironment. *J Clin Invest*. 2005;115(5):1163–1176.
19. Ginsberg MH, Partridge A, Shattil SJ. Integrin regulation. *Curr Opin Cell Biol*. 2005;17(5):509–516.
20. Bonaldo P, Braghetta P, Zanetti M, Piccolo S, Volpin D, Bressan GM. Collagen VI deficiency induces early onset myopathy in the mouse: an animal model for Bethlem myopathy. *Hum Mol Genet*. 1998;7(13):2135–2140.
21. Weisberg SP, McCann D, Desai M, Rosenbaum M, Leibel RL, Ferrante AW. Obesity is associated with macrophage accumulation in adipose tissue. *J Clin Invest*. 2003;112(12):1796–1808.
22. Hennighausen L, Robinson GW. Signaling pathways in mammary gland development. *Dev Cell*. 2001;1(4):467–475.
23. Lin EY, et al. Progression to malignancy in the polyoma middle T oncoprotein mouse breast cancer model provides a reliable model for human diseases. *Am J Pathol*. 2003;163(5):2113–2126.
24. Hanahan D, Weinberg RA. Hallmarks of cancer: the next generation. *Cell*. 2011;144(5):646–674.
25. Thiery JP. Epithelial-mesenchymal transitions in tumour progression. *Nat Rev Cancer*. 2002; 2(6):442–454.
26. Thiery JP, Sleeman JP. Complex networks orchestrate epithelial-mesenchymal transitions. *Nat Rev Mol Cell Biol*. 2006;7(2):131–142.
27. Massague J. TGF-beta signal transduction. *Annu Rev Biochem*. 1998;67:753–791.
28. Forrester E, et al. Effect of conditional knockout of the type II TGF-beta receptor gene in mammary epithelia on mammary gland development and polyomavirus middle T antigen induced tumor formation and metastasis. *Cancer Res*. 2005;65(6):2296–2302.
29. Muraoka-Cook RS, et al. Activated type I TGFbeta receptor kinase enhances the survival of mammary epithelial cells and accelerates tumor progression. *Oncogene*. 2006;25(24):3408–3423.
30. Muraoka-Cook RS, et al. Conditional overexpression of active transforming growth factor beta1 in vivo accelerates metastases of transgenic mammary tumors. *Cancer Res*. 2004;64(24):9002–9011.
31. Joyce JA, Pollard JW. Microenvironmental regulation of metastasis. *Nat Rev Cancer*. 2009;9(4):239–252.
32. Sun K, Kusminski CM, Scherer PE. Adipose tissue remodeling and obesity. *J Clin Invest*. 2011;121(6):2094–2101.
33. Halberg N, et al. Hypoxia-inducible factor 1alpha induces fibrosis and insulin resistance in white adipose tissue. *Mol Cell Biol*. 2009;29(16):4467–4483.
34. Khan T, et al. Metabolic dysregulation and adipose tissue fibrosis: role of collagen VI. *Mol Cell Biol*. 2009;29(6):1575–1591.
35. Nanda A, et al. TEM8 interacts with the cleaved C5 domain of collagen alpha 3(VI). *Cancer Res*. 2004;64(3):817–820.
36. Smith MJ, et al. Analysis of differential gene expression in colorectal cancer and stroma using fluorescence-activated cell sorting purification. *Br J Cancer*. 2009;100(9):1452–1464.
37. Arafat H, et al. Tumor-specific expression and alternative splicing of the COL6A3 gene in pancreatic cancer. *Surgery*. 2011;150(2):306–315.
38. Lai KK, et al. Extracellular matrix dynamics in hepatocarcinogenesis: a comparative proteomics study of PDGFC transgenic and Pten null mouse models. *PLoS Genet*. 2011;7(6):e1002147.
39. Levental KR, et al. Matrix crosslinking forces tumor progression by enhancing integrin signaling. *Cell*. 2009;139(5):891–906.
40. Naugle JE, et al. Type VI collagen induces cardiac myofibroblast differentiation: implications for postinfarction remodeling. *Am J Physiol Heart Circ Physiol*. 2006;290(1):H323–H330.
41. Atkinson JC, Ruhl M, Becker J, Ackermann R, Schuppan D. Collagen VI regulates normal and transformed mesenchymal cell proliferation in vitro. *Exp Cell Res*. 1996;228(2):283–291.
42. Pasarica M, et al. Adipose tissue collagen VI in obesity. *J Clin Endocrinol Metab*. 2009;94(12):5155–5162.
43. Spencer M, et al. Adipose tissue macrophages in insulin-resistant subjects are associated with collagen VI and fibrosis and demonstrate alternative activation. *Am J Physiol Endocrinol Metab*. 2010;299(6):E1016–E1027.
44. Maquoi E, Munaut C, Colige A, Collen D, Lijnen HR. Modulation of adipose tissue expression of murine matrix metalloproteinases and their tissue inhibitors with obesity. *Diabetes*. 2002;51(4):1093–1101.
45. Motrescu ER, et al. Matrix metalloproteinase-11/stromelysin-3 exhibits collagenolytic function against collagen VI under normal and malignant conditions. *Oncogene*. 2008;27(49):6347–6355.
46. Veidal SS, et al. MMP mediated degradation of type VI collagen is highly associated with liver fibrosis--identification and validation of a novel biochemical marker assay. *PLoS One*. 2011;6(9):e24753.
47. Overall CM, Lopez-Otin C. Strategies for MMP inhibition in cancer: innovations for the post-trial era. *Nat Rev Cancer*. 2002;2(9):657–672.
48. Gerling B, Becker M, Staab D, Schuppan D. Prediction of liver fibrosis according to serum collagen VI level in children with cystic fibrosis. *N Engl J Med*. 1997;336(22):1611–1612.
49. Zeichen J, van Griensven M, Albers I, Lobenhoffer P, Bosch U. Immunohistochemical localization of collagen VI in arthrofibrosis. *Arch Orthop Trauma Surg*. 1999;119(5–6):315–318.
50. Specks U, Nerlich A, Colby TV, Wiest I, Timpl R. Increased expression of type VI collagen in lung fibrosis. *Am J Respir Crit Care Med*. 1995;151(6):1956–1964.
51. Mollnau H, Munkel B, Schaper J. Collagen VI in the extracellular matrix of normal and failing human myocardium. *Herz*. 1995;20(2):89–94.
52. Park J, Kusminski CM, Chua SC, Scherer PE. Leptin receptor signaling supports cancer cell metabolism through suppression of mitochondrial respiration in vivo. *Am J Pathol*. 2010;177(6):3133–3144.